14

Monte Carlo Simulations of Semicrystalline Polyethylene: Interlamellar Domain and Crystal-Melt Interface

Markus Hütter[1], Pieter J. in 't Veld[2], and Gregory C. Rutledge[3]

[1] Department of Materials, ETH Zurich, CH-8093 Zurich, Switzerland, markus.huetter@mat.ethz.ch
[2] Sandia National Laboratories, Albuquerque, NM 87185, U.S.A., pjintve@sandia.gov
[3] Department of Chemical Engineering, Massachusetts Institute of Technology, Cambridge, MA 02139, U.S.A. rutledge@mit.edu

Abstract. The interlamellar domain of semicrystalline polyethylene is studied by means of off-lattice Metropolis Monte Carlo simulations using a realistic united atom force field with inclusion of torsional contributions. Both structural as well as thermal and mechanical properties are discussed for systems with the {201} crystal plane parallel to the interface. In so doing, important data is obtained which is useful for modeling semicrystalline polyethylene in terms of multiphase models. Here, we review the main results published previously by us [P.J. in 't Veld, M. Hütter, G.C. Rutledge: Macromolecules **39**, 439 (2006); M. Hütter, P.J. in 't Veld, G.C. Rutledge: Polymer (in press), (2006)].

On the one hand, the full interlamellar domain was characterized in terms of heat capacity, thermal expansion coefficients, Grüneisen coefficients, and the elastic compliance tensor at atmospheric pressure in the temperature range [350, 450] K. The simulation results corroborate the fact that the properties of the non-crystalline interlamellar phase lie between those of the amorphous melt and the semicrystalline solid, as quantitative comparison with experimental data shows. On the other hand, the interface between polyethylene crystal and melt is characterized in the temperature range [380, 450] K. We invoke the concept of the sharp Gibbs dividing surface to define and quantify the interface internal energy and the interface stresses. We find that the latter are in reasonable agreement with values derived from experimental data. By way of the Herring equation one can also infer that the surface tension of the fold surface is independent of shear strains in the interface.

14.1 Introduction, Motivation

Polymers are typically not fully crystalline below the melting temperature, due to frustration effects. As a result, a significant fraction of the sample consists of non-crystalline material between lamellae. These frustration effects

M. Hütter et al.: *Monte Carlo Simulations of Semicrystalline Polyethylene: Interlamellar Domain and Crystal-Melt Interface*, Lect. Notes Phys. **714**, 261–284 (2007)
DOI 10.1007/3-540-47307-6_14 © Springer-Verlag Berlin Heidelberg 2007

are particularly pronounced when the polymers are considerably longer than the lamella thickness. Chains then form bridges and loops, which are possibly entangled in the region between different lamellae, which in turn has ramifications also for the mechanical properties [1]. The characterization of this interlamellar domain is complicated by the presence and overlap of signals from several different phases and uncertainty in the assignment of a particular response to the interlamellar domain material [2,3]. In addition, in flexible and fast crystallizing polymers such as polyethylene (PE) where crystal phase relaxations are present, relationships between the crystal formation and the structure of the interlamellar material are obscured by fading memory [4]. It is also believed that the constraints imposed by the lamellae influence dramatically the dynamics of the interlamellar chain segments [5].

Two aspects, at least, of semicrystalline polymers must be discussed for arriving at a meaningful description, namely, structure and material properties. The effect of structure on the macroscopic material properties is described in many textbooks, e.g. by Torquato [6]. The importance of characterizing the structure is also realized in continuum modeling approaches, where powerful nonequilibrium thermodynamics techniques are used to incorporate structural information consistently into continuum models, which are then suitable for process modeling [7,8]. In particular, we mention the crystallization rate equations of [8] which not only separates the semicrystalline polymer into crystal and melt, but specifically distinguishes between the fold surfaces and growth surfaces of lamellae. In this way, information gained by microscopic studies can indeed be incorporated into descriptions on a different level. This being said, we address the material properties of the interlamellar domain and of the interface in the following.

Since a substantial amount of material is contained in the interlamellar region, the properties of the latter give significant contributions to the overall material behavior. The properties of the interlamellar material lie between those of the unconstrained amorphous melt and those of the crystalline phase [9–11], and the influence of the crystalline constraints can be addressed experimentally [12–14]. Furthermore, the properties of the crystal-melt interface have various ramifications that can be observed experimentally [15], e.g., interface stresses lead to distortion of the crystal lattice spacing [16–18], and they are possibly responsible for lamella twisting [19]. In addition, the surface tension enters in theoretical models for crystallization rates [20, 21].

To characterize the structure and to quantify the mechanical and thermal properties of the interlamellar, non-crystalline material, Metropolis Monte Carlo simulations have been performed [22–26] on systems kept in metastable equilibrium [27, 28]. Here, we give a summary of our most recent results for a realistic model for polyethylene including torsion interactions. For more details the reader is referred to the original publications [29, 30]. Throughout the manuscript, we concentrate our attention on the $\{201\}$ crystal surface, because it was found to be energetically favored in simulations [25] and predominant

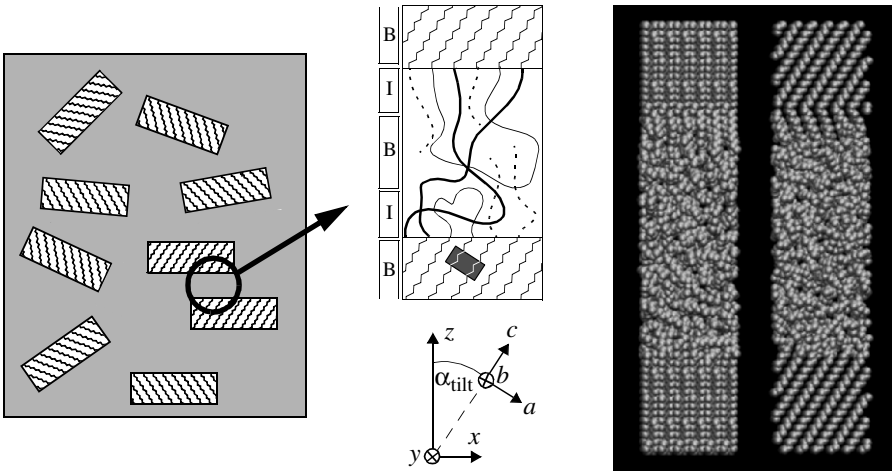

Fig. 14.1. Illustration of semicrystalline polyethylene on the *left*, consisting of crystalline lamellae and non-crystalline material (not necessarily indicative of actual morphology). The simulation box in the middle shows two crystalline lamellae and the interlamellar phase in between, which consists of loops (*thin solid lines*), bridge chains (*thick solid lines*), and tails (*dashed lines*). The polyethylene unit cell (*grey box, middle figure*) with coordinate axes (a, b, c) is tilted by an angle α_{tilt} with respect to the surface normal and the coordinate system (x, y, z). The bars with label "I" indicate the extended interface between crystalline and non-crystalline material, while "B" denotes regions with bulk-like properties, as explained in the text. On the right, snapshots are shown, viewing along the x- and y-direction, respectively

in experimental observations [31]. Figure 14.1 shows an illustration of the simulation box, as well as a snapshot of the simulations.

In the remainder of this contribution we study, on one hand, the entire interlamellar domain as a whole, termed "Study 1" [29]. On the other hand, the crystal-melt interface specifically is examined in "Study 2" [30]. In the course of explaining the results, the benefits of both of these approaches will become evident.

14.2 Methodology

14.2.1 Force Field, Virial Calculation of Stress

Polyethylene is modeled according to the united atom model of Paul et al. [32], as modified subsequently by Bolton et al. [33] and by In 't Veld and Rutledge [26], including the torsion angle terms. Using this force field, kinetic processes in semicrystalline PE have already been modeled accurately [34,35]. The stable crystal phase, though similar to that for PE, is actually pseudo-hexagonal.

Interactions both between non-bonded united atoms (CH_2) on different chain segments and between united atom pairs separated by four or more bonds in the same chain segment were calculated using a Lennard-Jones potential with a cut-off distance $r_c = 2.5\,\sigma_{LJ}$. In addition, three types of bonded interactions are included, accounting for the stiffness in the bond length, bond angle and torsion. The interaction potentials are, in that order,

$$E_{LJ,ij} = 4\varepsilon_{LJ}\left[\left(\frac{\sigma_{LJ}}{|\boldsymbol{d}_{i,j}|}\right)^{12} - \left(\frac{\sigma_{LJ}}{|\boldsymbol{d}_{i,j}|}\right)^{6}\right] , \tag{14.1}$$

$$E_{l,i} = \frac{1}{2}k_l\left(l_i - l_0\right)^2 , \tag{14.2}$$

$$E_{\theta,i} = \frac{1}{2}\frac{k_\theta}{\sin^2\theta_0}\left(\cos\theta_i - \cos\theta_0\right)^2 , \tag{14.3}$$

$$E_{\phi,i} = \sum_{n=0}^{3} k_n \cos^n\phi_i , \tag{14.4}$$

with parameters specified in Table 14.1, and $\boldsymbol{d}_{i,j} = \boldsymbol{r}_i - \boldsymbol{r}_j$ the distance between the Cartesian coordinates $\boldsymbol{r}_i$ and $\boldsymbol{r}_j$ of united atoms i and j. Furthermore, l_i is the length of bond i, θ_i is the complement of the bond angle constructed by bond i and $i-1$, and ϕ_i is the bond torsion angle constructed by the angle between the vectors $\boldsymbol{d}_{i,i-1} \times \boldsymbol{d}_{i-1,i-2}$ and $\boldsymbol{d}_{i-1,i-2} \times \boldsymbol{d}_{i-2,i-3}$.

For each of the force field contributions described above, there is a corresponding contribution to the total instantaneous stress tensor $\boldsymbol{\sigma}$, which is expressed in terms of the individual virial contributions. Explicit expressions for these contributions can be found in [26,29]. When using Lennard-Jones interactions for total energy calculations or for virial calculations of the stresses, long range corrections need to be included, as discussed by In 't Veld et al. [26].

14.2.2 Simulation Setup

Monte Carlo Simulation

The simulation box consisted of an immobile crystal phase and a mobile interlamellar phase – the combination of both interfacial material (covered by bars

Table 14.1. Parameters for the Interaction Potentials

Interaction	Parameter	Value
Lennard-Jones	ε_{LJ} (J/mol)	390.95
	σ_{LJ} (nm)	0.4009
Bond length	k_l (J/mol/nm^2)	376.1×10^6
	l_0 (nm)	0.1530
Bond angle	k_θ (kJ/mol)	502.1
	θ_0 (−)	68.0°
Bond torsion	$\{k_0, k_1, k_2, k_3\}$ (kJ/mol)	$\{6.498, -16.99, 3.626, 27.11\}$

"I" in Fig. 14.1) and truly amorphous material (middle bar "B" in Fig. 14.1) – as a model for semicrystalline polyethylene. The goal of studying the interface between crystal and melt also at temperatures different than the melting temperature requires that one imposes certain constraints on the system to keep the interlamellar domain in a metastable state [27]. Crystallization at low temperatures is prevented by keeping the volume constant, while in order to prevent melting at high temperatures the crystal sites are immobile.

Phase space is sampled in Metropolis Monte Carlo fashion by topology altering (end-reptation [36,37] and end-bridging [38]) and displacement (end-rotation [23], rebridging [39,40], and single-site displacement) moves [26], and parallel tempering [41] to facilitate more efficient sampling at low temperatures. For Study 1, the temperature profile according to the criteria in [41] is given by $T \in \{350, 359.9, 370.1, 380.6, 391.4, 402.4, 413.8, 425.6, 437.6, 450\}$ K. In Study 2 we used $T \in \{380.6, 391.4, 402.4, 413.8, 425.6, 437.6, 450\}$ K. An illustration of the simulation setup is given in Fig. 14.2.

Once created, the sufficient number of initial configurations generated as described below were randomized and then quenched, via intermediate temperatures, to the desired temperature profile, and equilibrated before any measurements were taken.

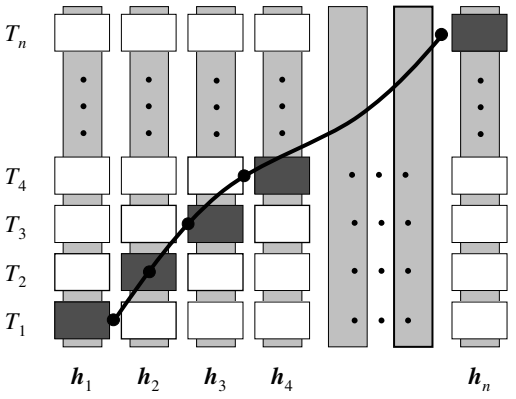

Fig. 14.2. Illustration of parallel tempering scheme as used in this study, with temperatures $\{T_1, \ldots, T_n\}$ and box geometries described by the tensors $\{\boldsymbol{h}_1, \ldots, \boldsymbol{h}_n\}$. Boxes represent simulated systems, each column denotes a parallel tempering simulation. The solid line represents $P = 1$ atm in the interlamellar phase as obtained by interpolation of the simulated data, and used in Study 1. For Study 2, the box geometries $\{\boldsymbol{h}_1, \ldots, \boldsymbol{h}_n\}$ are determined by the requirement of atmospheric conditions sufficiently far away from the interface into the crystal and melt, respectively, i.e., $P_c = P_m = 1$ atm

Crystal Unit Cell

It is widely known that united atom force fields lead to hexagonal symmetry of the crystal structure. However, they are quite accurate and efficient for simulation of amorphous structure. In our case of polyethylene, the united atom force field of Paul et al. leads to pseudo-hexagonal symmetry in the ab-plane, in contrast to the experimentally observed orthorhombic symmetry. Nevertheless, we deliberately accept this, because using a better force field in the crystal brings about the problem of how to transition between the two force fields at the interface. Also, the region of interest is not the crystal phase, but the interlamellar region.

In Study 1, the unit cell is adjusted to satisfy atmospheric pressure conditions at 400 K within the crystal phase. Specifically, the undeformed unit cell had $a = 0.77479\,\mathrm{nm}$, $b = 0.44626\,\mathrm{nm}$, and $c = 0.251822\,\mathrm{nm}$, with all crystallographic angles being 90 degrees. For Study 2, it was necessary to achieve atmospheric pressure conditions in the crystal at all temperatures considered, which can be achieved with unit cells with pseudo-hexagonal symmetry and lattice parameters $a(T) = (0.774053 + 0.0000471 \times (T - 400))\,\mathrm{nm}$, $b(T) = (0.445817 + 0.0000261 \times (T - 400))\,\mathrm{nm}$, and $c(T) = (0.252748 + 0.0000014 \times (T - 400))\,\mathrm{nm}$, where T is the temperature in units of K.

Simulation Box

The simulation box is illustrated in Fig. 14.1. It consists of the interlamellar phase enclosed between two lamellar crystals oriented with the {201} plane normal to the z-direction of the simulation cell.

Further specifications concerning the simulation cells used are summarized in Table 14.2, such as the dimensions of the rectangular simulation box, the thickness of the interlamellar domain $l_{z,\mathrm{il}}$, the number of tails n_{tail}, bridges n_{bridge} and loops n_{loop}. Here, we note that the Monte Carlo moves used keep both n_{tail} and the sum $n_{\mathrm{bridge}} + n_{\mathrm{loop}}$ constant. The loop and bridge populations are not constant individually but rather determined dynamically from

Table 14.2. Parameters and numbers as used in Study 1 and Study 2. The symbols are explained in the text. Quantities with a superscript star are temperature dependent, and only average values are reported in this table

	Study 1	Study 2
box size: (x, y, z) (nm)	$(2.77, 1.79, 8.72)$	$(2.77, 2.67, 12.64)$
$l_{z,\mathrm{il}}$ (nm)	7.66	7.22
n_{tail} $(-)$	12	18
$n_{\mathrm{bridge}} + n_{\mathrm{loop}}$ $(-)$	18	27
ρ_{il} (g/cc)	0.7947	0.79 *
N_{sites} $(-)$	1536	3750 *
$N_{\mathrm{sites,il}}$ $(-)$	1296	1950 *

the simulation. Notice also that the simulated lamellar surface is larger in Study 2 compared to Study 1, but the fraction $n_{\text{tail}}/(n_{\text{tail}} + n_{\text{bridge}} + n_{\text{loop}})$ is identical in both studies, i.e., the same surface is studied. The average mass density of the interlamellar domain, ρ_{il}, is adjusted in Study 1 in order to achieve atmospheric pressure conditions on average over the interlamellar domain at 402 K. In Study 2, we aimed at atmospheric conditions not on average but rather in regions where the influence of the interface is negligible, i.e., in the mid-plane of the simulation box. The total number of sites in the entire simulation cell and in the interlamellar domain are denoted by N_{sites} and $N_{\text{sites,il}}$, respectively.

Keeping in mind that only the relevant surface region of the lamellae in the simulation cell in Fig. 14.1 is shown and needed for the simulation, these simulations are representative of semicrystalline morphologies having thicker crystal lamellae. Assuming realistic lamellae thicknesses, our simulation parameters can be translated into an estimate of the molecular weight of the polyethylene, $M_{\text{w}} \sim 10^4\,\text{g/mol}$, and a degree of crystallinity, $\phi_{\text{c}} \sim 62\%$, as shown in [27]. Thus, the crystallinity and lamellar spacing studied here are comparable to the values cited by Hoffman [42] and Crist et al. [14].

For purposes of elastic property calculations, tensile and compressive deformations were simulated at ε_i $(i = 1, 2, 3)$ in the interval $[-8.75\%, 8.75\%]$ in steps of 1.25%, with a few unimportant exceptions. Combined tensile deformations, used in calculation of the off-diagonal stiffness coefficients, were simulated for values of pairs $\{\varepsilon_i, \varepsilon_j\}$ $(i, j = 1, 2, 3; i \neq j)$ with magnitudes $\varepsilon_i = \varepsilon_j$ in the range $[-4.375\%, 4.375\%]$ with increments of 0.625%. Shear deformations were performed under simple shear for ε_i $(i = 4, 5, 6)$ in the range $[-5\%, 5\%]$ in steps of 1.25%.

14.2.3 Thermal and Elastic Properties of Interlamellar Domain

The calculation of elastic properties in Study 1 was performed by simulations in the $N\boldsymbol{h}T$-ensemble for specific values of T and $\boldsymbol{h}$ (see Fig. 14.2). Here, $\boldsymbol{h}$ is the tensor that describes both the size and shape of the system, e.g. $V = \det(\boldsymbol{h})$ [43]. At each point $(T, \boldsymbol{h})$, the pressure is calculated as $P = -\text{Tr}\,[\boldsymbol{\sigma}(T, \boldsymbol{h})/3]$. Since our focus is on the interlamellar domain, stress contributions from the rigid crystals are not included in Study 1. Lines of constant pressure can thus be obtained through interpolation. In Fig. 14.2, the solid line is a schematic representation of the condition $P = 1\,\text{atm}$. The pressure in the interlamellar domain at each temperature can be adjusted by varying only that component of $\boldsymbol{h}$ which describes the interlamellar thickness perpendicular to the interface. In the other two orthogonal directions in the interface plane, the extension of the interlamellar domain is more rigidly constrained due to continuity with the crystal lattice. The condition $P = 1\,\text{atm}$ leads to a relation between cell volume and temperature, $V_0(T)$. Any property X can hence be considered in terms of $X(V, T)$ or $X(P, T)$. In particular, temperature derivatives at constant volume, $(\partial X(V, T)/\partial T)|_V$

(along vertical lines in Fig. 14.2), and at constant pressure $P = 1\,\mathrm{atm}$, $(\partial X(P,T)/\partial T)|_P = (dX(V_0(T),T)/dT)$ (along the solid line in Fig. 14.2), can be calculated.

After appropriate interpolation procedures [29], isochoric and isobaric heat capacities at atmospheric pressure were calculated,

$$C_V = (\partial E/\partial T)|_V \ , \tag{14.5}$$

$$C_P = (\partial E/\partial T)|_P + P\,(\partial V/\partial T)|_P \ . \tag{14.6}$$

Furthermore, stresses were calculated as functions of strain and temperature. For each temperature, each component of stress was fit to a second order Taylor series expansion in terms of the strains, about the $P = 1\,\mathrm{atm}$ reference volume $V_0(T)$ at each specific temperature. Based on the stresses, the elastic moduli C_{ij} and the Grüneisen coefficients γ_i $(i = 1, 2, 3)$ of the non-crystalline interlamellar phase were calculated using

$$C_{ij} = (\partial\sigma_i/\partial\varepsilon_j)|_{T,\varepsilon_{k\neq j}} \ , \tag{14.7}$$

$$\gamma_i = -V_0\,C_V^{-1}\ (\partial\sigma_i/\partial T)|_{V=V_0} = C_V^{-1}\ (\partial S/\partial\varepsilon_i)|_{T,\varepsilon_{k\neq i}} \ , \tag{14.8}$$

where the Voigt notation is used throughout the manuscript. The Grüneisen coefficients provide a measure of entropic contributions to the elastic moduli.

14.2.4 Energy and Stresses in the Crystal-Melt Interface

Chain connectivity between the crystalline and non-crystalline domains and the finite stiffness of polyethylene result in a finite thickness of the transition region that has no counterpart in the crystal-liquid interface for low molecular weight substances. On the molecular scale, this transition region extends well beyond what may be regarded as the surface of the crystal phase, prompting use of the term "interphase" to describe this transition region [44]. For thermodynamic purposes, however, it is convenient to characterize the properties of this interphase as those associated with an interfacial dividing surface. In order to approximate this region (termed "I" in Fig. 14.1) using a sharp interface, a coarse-graining step is involved. The procedure adopted here uses the concept of the Gibbs dividing surface [45–47].

The finite width of the transition region is reflected in the position dependent profiles of mass density $\rho(z)$, internal energy density $e(z)$ and stress tensor $\boldsymbol{\sigma}(z)$, which can all be obtained from Monte Carlo simulations. In accord with these profiles as a function of the coordinate z along the surface normal, one can define the corresponding properties of the interface,

$$\rho_{\mathrm{int}} := \int_{-\infty}^{\infty} \left[\rho(z) - \rho^{\mathrm{step}}(z)\right] dz \ , \tag{14.9}$$

$$e_{\mathrm{int}} := \int_{-\infty}^{\infty} \left[e(z) - e^{\mathrm{step}}(z)\right] dz \ , \tag{14.10}$$

$$\pi_{\alpha\beta} := \int_{-\infty}^{\infty} \left[\sigma_{\alpha\beta}(z) - \sigma_{\alpha\beta}^{\mathrm{step}}(z)\right] dz \qquad (\alpha,\beta = x,y) \ . \tag{14.11}$$

Each quantity with superscript "step" denotes a Heaviside step function which on either side of the step takes the values identical to the corresponding bulk values of the crystal and melt domains sufficiently far away from the transition region. Therefore, regions far away from the interface do not contribute to the integrals, i.e., the integrand approaches zero rapidly. The criterion of a massless interface, $\rho_{\mathrm{int}} = 0$, determines the position of the step, i.e., the position of the Gibbs dividing surface, z_{div}. The latter is then used also in the step functions for e_{int} and $\pi_{\alpha\beta}$, see Fig. 14.3. The physical interpretation of the interface properties given by (14.9-14.11) as 'excess quantities' is now obvious: It is the differences between the real profile and the extrapolation of the bulk values up to the sharp interface. In that sense, they isolate the effect of the interface. We note that determination of the surface tension γ, i.e., the Helmholtz free energy per unit area, from the interface stresses is non-trivial, as expressed by the Herring equation [18, 48, 49]

$$\pi_{\alpha\beta} = \gamma\delta_{\alpha\beta} + \left.\frac{\partial\gamma}{\partial\varepsilon_{\alpha\beta}}\right|_T , \tag{14.12}$$

where $\delta_{\alpha\beta}$ denotes the identity matrix. Because one of the adjoining phases is solid, γ depends on the strain in the interface, $\varepsilon_{\alpha\beta}$ $(\alpha, \beta = x, y)$.

Since the crystal-melt interface under consideration has zero curvature, it is natural to assume that atmospheric pressure conditions prevail sufficiently far away from the interface, putting constraints on the lattice parameters of the pseudo-hexagonal unit cell, and on the interlamellar domain. All these parameters of the box geometry are included in the label $\boldsymbol{h}$ in Fig. 14.2. Dark

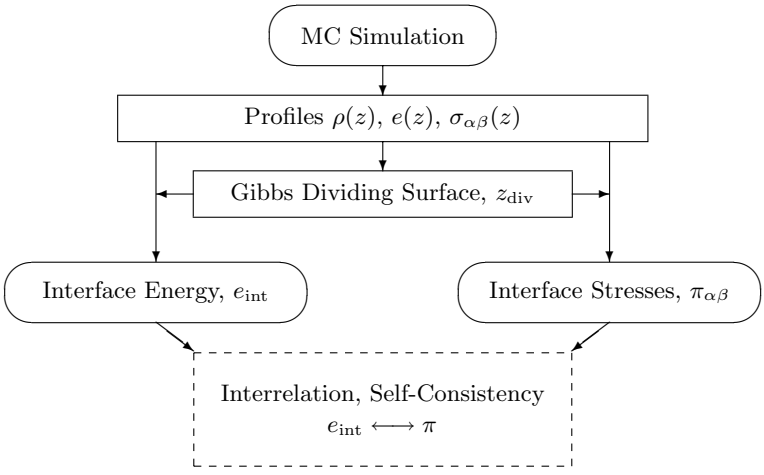

Fig. 14.3. Illustration of the procedure to calculate interface internal energy, e_{int}, and the interface stresses, $\pi_{\alpha\beta}$, as used here for the polyethylene {201} crystal surface

boxes indicate the systems in which atmospheric conditions are established in the bulk crystal and melt domains, respectively.

14.3 Results and Discussion

14.3.1 Conformational Properties

The average lengths of bridge, loop and tail segments in the interlamellar phase as functions of temperature were investigated in Study 1. In the simulation procedure, the probability for attachment and removal of a single CH_2 group is independent of the chain length n, and hence one can anticipate that the chemical potential for a chain segment of n united atoms takes the form $\mu(n,T) = \mu_0(T) + \mu_n(T)n$ with $\mu_n(T) > 0$. As a consequence, the loop, bridge and tail distributions should depend exponentially on n, i.e., $p(n,T) \sim \exp[-\mu(n,T)/k_\mathrm{B}T]$ for sufficiently large n, in agreement with our simulation results (not shown).

As far as the temperature dependence of the average segment length is concerned, one finds that it increases with temperature for both bridge and tail populations, from $\langle n_\mathrm{bridge}\rangle \approx 139$ and $\langle n_\mathrm{tail}\rangle \approx 44$ at 350 K to $\langle n_\mathrm{bridge}\rangle \approx 169$ and $\langle n_\mathrm{tail}\rangle \approx 55$ at 450 K. These temperature dependences originate primarily from the factor $1/T$ in the exponential of the distribution function. In contrast, for loops one observes a slight decrease in average length with increasing temperature, from $\langle n_\mathrm{loop}\rangle \approx 36$ at 350 K to $\langle n_\mathrm{loop}\rangle \approx 30$ at 450 K. This reverse trend is attributed to torsional hindrances, which become more stringent the shorter the loops. Hence, we conclude that the temperature dependence of $\mu_n(T)$ is significant in the case of loops, due to torsional contributions.

Next, we consider the equilibrium topology, i.e., the relaxed state long after crystallization has stopped, of the {201} crystal/amorphous interface in polyethylene, which has ramifications for material properties of the interlamellar phase. In particular, we focus on the statistics of loops. We abbreviate with $[mn0]$ the reentry vector or end-to-end vector for a loop segment, $[\pm m\,l_x, \pm n\,l_y, 0]$, with l_x and l_y representing the projected length of a unit cell vector (a or b) at the crystal surface in the x- and y-directions, respectively. Figure 14.4 shows results at temperatures 350 K and 450 K, where the length of the reentry vector increases from left to right, and n is assumed to be integer. Firstly, one observes that loops with reentry vectors oriented along $[0\,n\,0]$ are the most common. This population is dominated by the $[0\,1\,0]$ loops, which are the shortest of all possible loops in the {201} interface for the pseudo-hexagonal unit cell considered here. Secondly, the loop populations decrease with increasing distance between reentry points. Thirdly, the "rest" population is comprised exclusively of loops with reentry vectors longer than that for the $[1\,1\,0]$ direction. Comparison of the results for PE and the freely-rotating chain (FRC) show that the torsion leads to longer loops [29]. This is

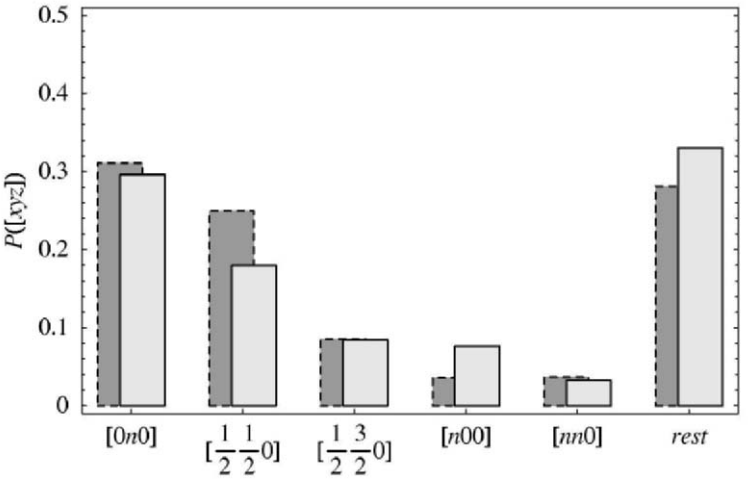

Fig. 14.4. Reentry distribution at the undeformed state of polyethylene as a function of reentry orientation at two temperatures; light bar: 350K, dark bar: 450K. The last entry "rest" lumps together all the remaining loops not explicitly considered in the other sets. The shortest reentry vector length in a particular direction increases from left to right. See text for notation. Reproduced from [29] with written permission from ACS Publications

in accord with our observation above that the loop length distribution is substantially influenced by the torsion potential. Lastly, Fig. 14.4 indicates that reconstruction of reentry topology associated with changes in temperature between 350 K and 450 K has a relatively small effect.

14.3.2 Thermal and Elastic Properties of Interlamellar Domain

In this subsection, the interlamellar domain is characterized in terms of thermal and elastic properties, as obtained from our Study 1 MC simulations. The most important results are summarized in Table 14.3.

Isochoric and Isobaric Heat Capacities

The isochoric and isobaric heat capacities of the interlamellar domain are displayed in Fig. 14.5 as functions of temperature at atmospheric pressure. In terms of the scheme in Fig. 14.2, isochoric temperature derivatives describe changes along vertical columns of constant $\boldsymbol{h}$ evaluated on the solid line representing $P = 1\,\text{atm}$, while isobaric temperature derivatives capture changes along the line $P = 1\,\text{atm}$. The isochoric heat capacity $C_V(T)$ at $P = 1\,\text{atm}$ is of the order of $26\,\text{J/K/mol}\,\text{CH}_2$, which was also checked using the fluctuation formula [50] with consistent results. The isobaric heat capacity $C_P(T)$

Table 14.3. Summary of the properties of the interlamellar phase and of the sharp interface, as discussed in the text. Superscripts: values from Study 1 at $P = 1\,\mathrm{atm}$ (a1) in the temperature range $[350, 450]\,\mathrm{K}$, (a1-) in the temperature range $[360, 450]\,\mathrm{K}$, and (b) at $T = 435\,\mathrm{K}$; (a2) denotes values from Study 2 in the temperature range $[380.6, 450]\,\mathrm{K}$ and $P_\mathrm{c} = P_\mathrm{m} = 1\,\mathrm{atm}$. For ranges of temperature, we give only the values of that specific property at the lowest and at the highest temperature. Note that all properties summarized here have a monotonic temperature dependence in the temperature range given, except for C_V and α_3, which both have a shallow maximum

	Property	Value
Interlamellar Domain	C_V (J/K/mol CH_2)	$[25.0 \pm 0.8, 25.5 \pm 0.3]$ (a1)
	C_P (J/K/mol CH_2)	$[32.7 \pm 0.2, 31.8 \pm 0.2]$ (a1)
	$\{E_1, E_2, E_3\}$ (GPa)	$\{0.49, 0.77, 0.27\}$ (b)
	$\{G_1, G_2, G_3\}$ (GPa)	$\{-0.17, 0.12, 1.17\}$ (b)
	K (GPa)	0.89 (b)
	γ_1 $(-)$	$[0.77 \pm 0.04, 0.43 \pm 0.01]$ (a1)
	γ_2 $(-)$	$[0.74 \pm 0.03, 0.44 \pm 0.02]$ (a1)
	γ_3 $(-)$	$[0.77 \pm 0.04, 0.43 \pm 0.02]$ (a1)
	α_1 $(10^{-4}/\mathrm{K})$	$[2.38, 0.41]$ (a1−)
	α_2 $(10^{-4}/\mathrm{K})$	$[-0.45, 0.27]$ (a1−)
	α_3 $(10^{-4}/\mathrm{K})$	$[6.54, 6.49]$ (a1−)
Crystal-Melt Interface	e_int $(\mathrm{J/m^2})$	$[0.299 \pm 0.006, 0.340 \pm 0.004]$ (a2)
	$(\partial e_\mathrm{int}/\partial T)\vert_{\boldsymbol{h}}$ $(10^{-3}\mathrm{J/m^2/K})$	$[-2.5 \pm 0.6, 0.9 \pm 0.2]$ (a2)
	π_{xx} $(\mathrm{J/m^2})$	$[-0.293 \pm 0.009, -0.244 \pm 0.007]$ (a2)
	π_{yy} $(\mathrm{J/m^2})$	$[-0.379 \pm 0.008, -0.428 \pm 0.007]$ (a2)
	π_{xy} $(\mathrm{J/m^2})$	$\sim 0 \pm 0.006$ (a2)

at $P = 1\,\mathrm{atm}$ is of the order $32\,\mathrm{J/K/mol\,CH_2}$, i.e., approx. 20% larger than $C_V(T)$, but slightly lower compared to extrapolated experimental values of an amorphous polyethylene melt (from $33.1\,\mathrm{J/K/mol\,CH_2}$ to $37.8\,\mathrm{J/K/mol\,CH_2}$) at the same pressure and temperatures [51].

Elastic Stiffness and Compliance, Stability

In Fig. 14.6, tensile ($i, j = 1, 2, 3$) and shear ($i, j = 4, 5, 6$) components C_{ij} of the stiffness matrix (Voigt notation) at constant pressure are shown. In

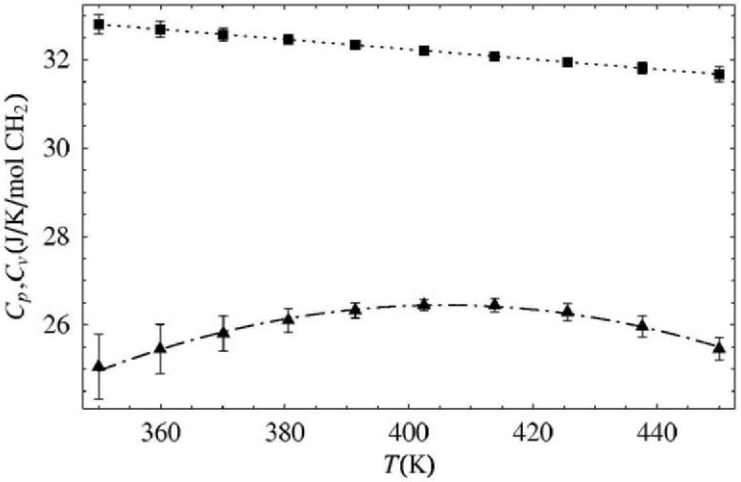

Fig. 14.5. Heat capacities at atmospheric pressure; ■: C_p; ▲: C_V. Reproduced from [29] with written permission from ACS Publications

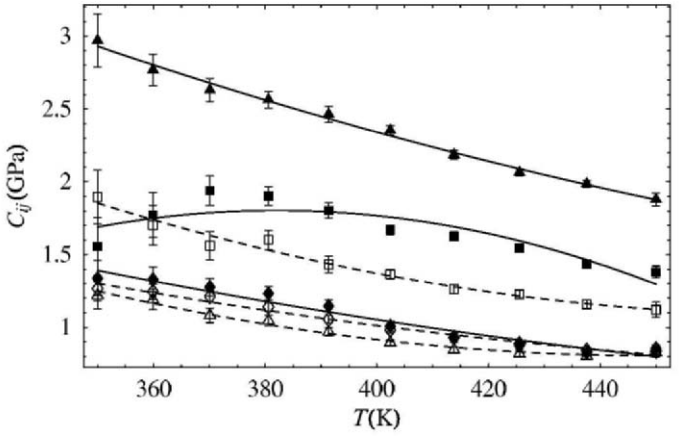

Fig. 14.6. Tensile and shear contributions to the elastic stiffness matrix C at atmospheric pressure; ■: C_{11}; ▲: C_{22}; ♦: C_{33}; □: C_{12}; △: C_{13}; ◊: C_{23}. Lines are drawn as a guide to the eye. Reproduced from [29] with written permission from ACS Publications

general, they decrease with increasing temperature, as expected [52]. The shear components were calculated as functions of temperature, but only for deformation about a single reference cell, $\boldsymbol{h}_0$ at $T = 435\,\mathrm{K}$. For that temperature, we can report the full stiffness tensor C for the non-crystalline interlamellar material in PE at $P = 1\,\mathrm{atm}$ (in GPa):

$$\mathsf{C} = \begin{pmatrix} 1.54 & 1.21 & 0.83 & 0.00 & -0.18 & 0.00 \\ 1.21 & 2.02 & 0.87 & 0.00 & -0.24 & 0.00 \\ 0.83 & 0.87 & 0.90 & 0.00 & 0.05 & 0.00 \\ 0.00 & 0.00 & 0.00 & \sim 0.00 & 0.00 & -0.20 \\ -0.18 & -0.24 & 0.05 & 0.00 & 0.22 & 0.00 \\ 0.00 & 0.00 & 0.00 & -0.20 & 0.00 & 0.57 \end{pmatrix} . \tag{14.13}$$

This stiffness tensor has monoclinic symmetry rather than pseudo-hexagonal, since the underlying pseudo-hexagonal crystal is tilted away from the c-axis. The uncertainty in each of the tensile stiffnesses is ± 0.03 GPa; the uncertainty in each of the shear stiffnesses is ± 0.06 GPa, with the exception of C_{44}, where the uncertainty is closer to ± 0.1 GPa. Within the accuracy of our sampling, C_{44} is zero within errors. As a consequence the system is at best only marginally stable, since the determinant of the stiffness matrix in (14.13) is close to zero.

The best estimate of the elastic compliance matrix S at $P = 1$ atm and $T = 435$ K is obtained by inversion of the stiffness matrix and using standard propagation of errors. One obtains for S (in GPa^{-1})

$$\mathsf{S} = \begin{pmatrix} 2.0 & -0.34 & -1.6 & 0. & 1.6 & 0. \\ -0.34 & 1.3 & -1.0 & 0. & 1.3 & 0. \\ -1.6 & -1.0 & 3.7 & 0. & -3.2 & 0. \\ 0. & 0. & 0. & -6.0 & 0. & -2.3 \\ 1.6 & 1.3 & -3.2 & 0.0 & 8.3 & 0. \\ 0. & 0. & 0. & -2.3 & 0. & 0.85 \end{pmatrix} . \tag{14.14}$$

The uncertainty in C_{44} does not affect most of the compliances, but it does result in unreliable values for S_{44} and S_{66}. From (14.14), we estimate the Young's moduli $E_i = 1/S_{ii}$ $(i = 1, 2, 3)$, the shear moduli $G_{i-3} = 1/S_{ii}$ $(i = 4, 5, 6)$, and the bulk modulus $K = 1/((S_{11} + S_{22} + S_{33}) + 2(S_{12} + S_{13} + S_{23}))$ [53], with values reported in Table 14.3. Due to the aforementioned uncertainty in C_{44}, the results for G_1 and G_3 should be interpreted with caution. We also mention that Krigas et al. reported shear modulus data for the fully amorphous melt below the detection limit of our simulations, explaining our difficulty in determining an accurate value of G_1 [54]. The results for the Young's moduli are similar to experimental values between 0.02 GPa and 0.4 GPa estimated by Crist et al. [14]. Reported experimental bulk moduli for a PE melt range from 1.38 GPa to 0.87 GPa at 350 K to 450 K, respectively, and from 3.37 GPa to an extrapolated value of 0.84 GPa for semicrystalline PE at the same temperatures [52]. Due to the connectivity between the crystal and the interlamellar material, the latter is expected to be stiffer than the pure melt.

The entropic contributions to the elastic moduli (see Fig. 14.6) is given by the Grüneisen parameters, which show a close to linear temperature dependence in our simulations, ranging from ~ 0.75 at 350 K to 0.4 at 450 K. These results are lower than our previous results [26] which ignored torsion

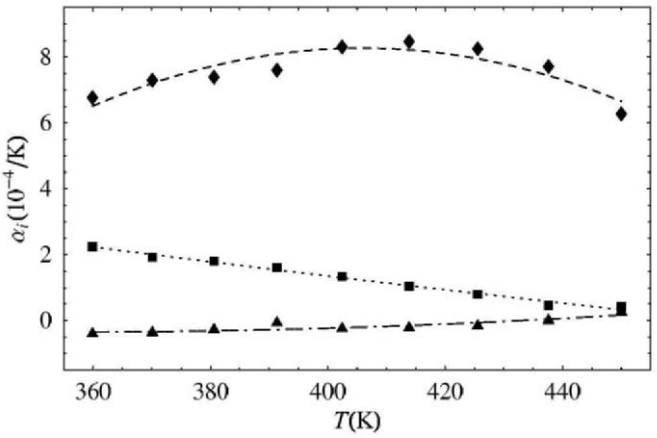

Fig. 14.7. Thermal expansion coefficients as functions of temperature at atmospheric pressure; ■: α_1; ▲: α_2; ♦: α_3. Reproduced from [29] with written permission from ACS Publications

contributions and where the average interlamellar pressures ($1300-2500$ atm) were substantially different from the one used here (1 atm).

Coefficients of Thermal Expansion

The coefficients of linear thermal expansion are reported in Fig. 14.7 as functions of temperature. The method to their calculation is described elsewhere [26], under the assumption that $\gamma_5 \ll \gamma_{1,2\,\text{or}\,3}$, and interpolated to volumes corresponding to atmospheric pressure conditions. Experimental data for linear thermal expansion coefficients for the amorphous melt range from 7.11×10^{-4}/K to 7.23×10^{-4}/K under comparable conditions [55]. We emphasize that this agrees nicely with the simulated value for α_3 shown in Fig. 14.7. While the thermal expansion in the direction normal to the crystal surface is not immediately constrained by the crystal, it is substantially decreased in the xy-plane due to chain continuity, in accord with the data for α_1 and α_2 reported in Fig. 14.7.

14.3.3 Properties of the Crystal-Melt Interface

Much of the interesting physics in semicrystalline materials is hidden in the transition region between the crystalline domain and the melt-like domain. In particular in polymeric systems with a certain degree of stiffness of the backbone, the chain connectivity between both phases results in a rather wide transition region. In the following, we focus on the characterization of the crystal-melt interface by invoking the Gibbs construction of a sharp

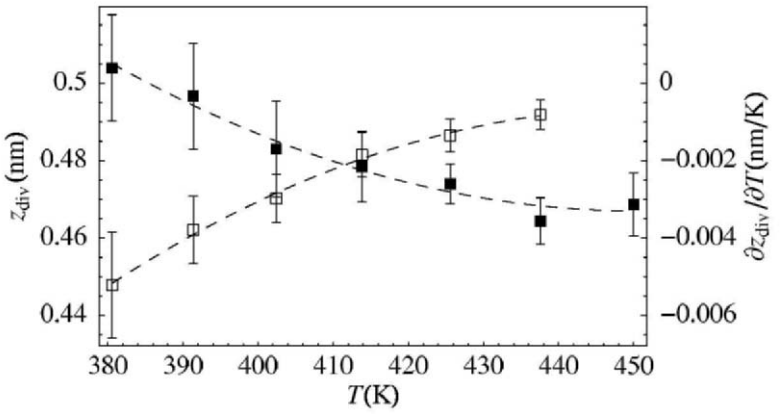

Fig. 14.8. Position of the Gibbs dividing surface z_{div} plotted versus temperature T at atmospheric conditions in the bulk phases, $P_{\mathrm{c}} = P_{\mathrm{m}} = 1\,\mathrm{atm}$ (■), and its temperature derivative at constant box geometry, $(\partial z_{\mathrm{div}}/\partial T)|_{\boldsymbol{h}}$ (□). Reprinted from [30] with written permission from Elsevier

dividing surface. The most important quantitative results are summarized in Table 14.3.

Position of the Gibbs Dividing Surface

The calculation of the interface properties as described in Sect. 14.2.4 requires determination of the position of the Gibbs dividing surface, z_{div}. We calculated the mass density profiles $\rho(z)$, and then used the criterion $\rho_{\mathrm{int}} = 0$ with (14.9). The resulting values are reported in Fig. 14.8. There, the position of the Gibbs dividing surface is measured with respect to the real crystal surface, which is defined midway between the top layer of united atoms in the crystal and the first layer of mobile atoms bonded to it. The thickness of the interface (approx. equal to $2z_{\mathrm{div}}$) decreases for the higher temperatures as a result of weakened chain stiffness and entropic effects, in accord with previous results [26].

The derivative of z_{div} at constant bulk pressures (i.e., along the diagonal in Fig. 14.2) as obtained from Fig. 14.8 (■) goes from approximately -9×10^{-4}nm/K below $T = 400\,\mathrm{K}$ to zero within error bars above $T = 430\,\mathrm{K}$. On the other hand, the derivative at constant box geometry (i.e., along vertical lines in Fig. 14.2) are about a factor of six larger (□ in Fig. 14.8). We believe that this is explained by the fact that increasing the temperature at constant box geometry leads to increased pressure in the melt phase, which in turn further compresses the interface. Therefore, this additional effect leads to larger values for $(\partial z_{\mathrm{div}}/\partial T)|_{\boldsymbol{h}}$ in comparison to $(\partial z_{\mathrm{div}}/\partial T)|_{P_{\mathrm{c}}=P_{\mathrm{m}}=1\,\mathrm{atm}}$.

The error bars in Fig. 14.8 (as also for Figs. 14.9 and 14.10) are calculated by splitting the entire Monte Carlo simulation in ten blocks, from which

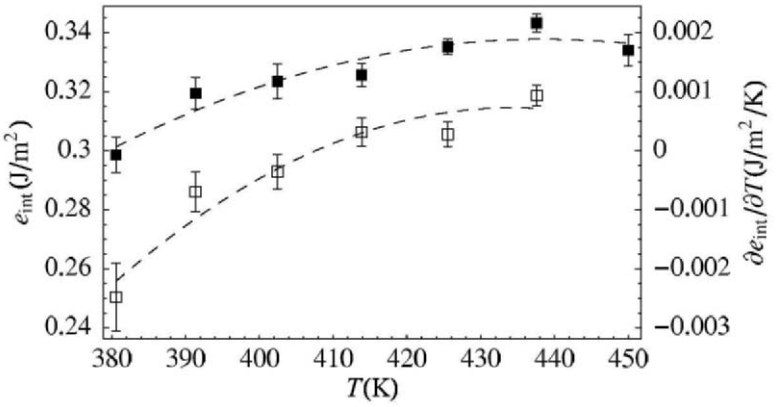

Fig. 14.9. Interface internal energy $e_{\rm int}$ plotted versus temperature T at $P_{\rm c} = P_{\rm m} = 1\,{\rm atm}$ (■), and its temperature derivative at constant interface strain and constant system volume, $(\partial e_{\rm int}/\partial T)|_{\boldsymbol{h}}$ (□). Reprinted from [30] with written permission from Elsevier

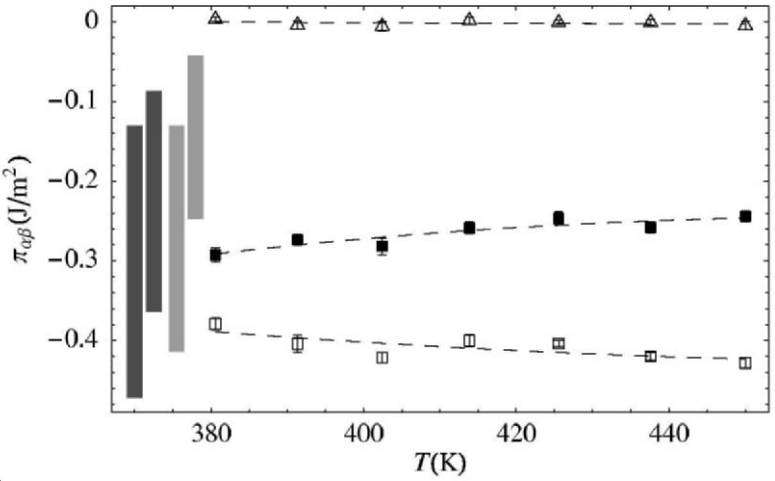

Fig. 14.10. Interface stresses, plotted versus temperature at atmospheric bulk stresses in the adjoining crystal and melt phases: π_{xx} (■), π_{yy} (□), and π_{xy} (△). *Solid bars* indicate the ranges of values given in [16–18] for n-paraffin at $T = 296\,{\rm K}$ (*dark grey*), and melt-crystallized polyethylene at $T = 298\,{\rm K}$ (*light grey*). Reprinted from [30] with written permission from Elsevier

ten statistically independent block averages are calculated. In turn, these ten averages are used to determine the total average and the associated error. Propagation of errors is employed to obtain the error of the temperature

derivatives, based on the three successive data points used for the calculation of the slope.

14.3.4 Internal Energy of the Interface

The internal energy of the interface can be calculated in our MC simulations according to (14.10), with the aid of the position of the Gibbs dividing surface, z_{div} (see Fig. 14.3). The results are shown in Fig. 14.9 (■). The interface energy increases steadily from $0.30\,\mathrm{J/m^2}$ at 380 K to $\sim 0.335\,\mathrm{J/m^2}$ at the melting temperature ($T_{\mathrm{m}} \simeq 410\,\mathrm{K}$), and remains approximately constant above.

The temperature derivative of the interface energy is particularly interesting. We have mentioned in the previous section the difference between temperature derivatives at constant bulk pressures in contrast to constant box geometry. Although the fact that they are different may not come as a surprise, it is unexpected that these two types of temperature derivatives may even have opposite sign, as illustrated in the following. While the derivative at constant bulk pressure (change along the diagonal in Fig. 14.2) has a positive slope according to the data in Fig. 14.9 (■) at low temperatures, the derivative at constant box geometry (change along columns in Fig. 14.2) is negative below the melting temperature (□ in Fig. 14.9). An explanation for the different signs of the slopes needs to take into account that the temperature derivative of the interface energy depends not only on the profile $e(z)$, but also on z_{div}, which in turn originates from the profile $\rho(z)$. For a detailed explanation the reader is referred to [30].

As shown in detail in [30], the heat capacity at constant total volume of semicrystalline polyethylene contains phase change contributions due to a change in volume fraction (here, $\partial z_{\mathrm{div}}/\partial T|_{\boldsymbol{h}}$) and due to a change in the internal energy of the interface (here, $\partial e_{\mathrm{int}}/\partial T|_{\boldsymbol{h}}$), which is the reason for calling the heat capacity of semicrystalline polymers "apparent". We mention that we refrain from calling $(\partial e_{\mathrm{int}}/\partial T)|_{\boldsymbol{h}}$ a "heat capacity at constant surface area" of the interface, as suggested by analogy to its bulk counterpart "heat capacity at constant volume". We recall that e_{int} is an excess property by definition, and its behavior upon changing temperature is strongly interwoven with the thermodynamic behavior of the two adjoining bulk phases.

14.3.5 Interface Stresses

The values for the interface stresses calculated according to (14.11) for $P_{\mathrm{c}} = P_{\mathrm{m}} = 1\,\mathrm{atm}$ (i.e., on the diagonal of the schematic in Fig. 14.2) are reported in Fig. 14.10.

Two features of the data in Fig. 14.10 are striking, namely the sign of the diagonal stresses and the anisotropy. The fact that the interface stresses are negative means that the interface tries to expand, which can be rationalized with these two arguments. Firstly, the chains are in perfect crystalline registry in the crystal domain, but then the chains exit the crystal and attempt to gain

more configurational entropy, i.e., they exert pressure on each other to gain more space. Secondly, (short) folds preferentially try to increase the distance between anchor points due to the stiffness of the backbone. Our results are of the same order of magnitude as the ones reported by Cammarata, Eby and Fisher [16–18], which are between $-0.1\,\mathrm{J/m^2}$ and $-0.3\,\mathrm{J/m^2}$ for the {001} surface.

By virtue of the Herring equation (14.12), measurements of the surface tension of the fold surface are also interesting, which in turn enters in theoretical models for experimentally measurable crystallization rates [20,21]. In view of the interface stress values in Fig. 14.10 it is interesting to note that experimental values for the scalar surface tension are in the range $\gamma = +0.1\,\mathrm{J/m^2}$. The fact that these values are of the same order of magnitude as the interface stresses, but with opposite sign, draws attention to the strain dependence of the surface tension in the Herring equation (14.12). For the diagonal components, the term $(\partial\gamma/\partial\varepsilon_{\alpha\alpha})|_T$ over-compensates the isotropic contribution γ by far, which serves as a measure of the strong dependence of the surface tension on tensile strains. We also observe $|\pi_{xx}|, |\pi_{yy}| > \gamma$, which we suppose to be related to the presence of short folds [15]. This is in agreement with our simulations for which the average loop length is rather short, as reported in Sect. 14.3.1

The off-diagonal stress π_{xy} is zero within error, according to Fig. 14.10. From this one can conclude that the scalar surface tension is independent of small shear deformations in the plane of the interface, as can be inferred from the Herring equation (14.12).

The rigorous definition of the interface stresses relies on mechanical equilibrium, i.e., the shear stresses in the out-of-plane directions being zero and σ_{zz} independent of z. In order to measure such effects in our simulations in relation to the in-plane interface stresses, the definition (14.11) is also applied to the out-of-plane components of the stress profile. One finds that $|\pi_{xz}| \lesssim 0.05\,\mathrm{J/m^2}$, $|\pi_{yz}| \lesssim 0.01\,\mathrm{J/m^2}$, and $|\pi_{zz}| \lesssim 0.05\,\mathrm{J/m^2}$. Hence, the stress integrals involving the z-direction are 20% or less in magnitude compared to π_{xx}, and even smaller when compared to π_{yy}. Nevertheless, they are significant, and we believe that the stresses π_{xz} and π_{zz} are a signature of the tilted chains exiting the crystal with a certain persistence along the backbone.

14.4 Summary and Discussion

The structural, thermal and mechanical characterization of the interlamellar domain and of the {201} crystal-melt interface of semicrystalline PE was performed, and compared with experimental data where available. Monte Carlo simulations complete with three-fold torsional potential were used with a united atom representation of polyethylene. We have employed two different strategies to assess the properties of the interface.

14.4.1 Entire Interlamellar Domain

The morphology was quantified in terms of loop reentry distributions and the average lengths of loops, bridge molecules, and dangling chain ends, i.e., tails. The distribution of reentry vectors on the {201} surface of PE showed that the shorter the reentry vector the more probable its occurrence. In particular, the shortest reentry vector [0 1 0] was the most common. We found that the length distribution of the different types of segments (loops, bridges, tails) over a large range decays exponentially with segment length, i.e., that the chemical potential, μ_n, for addition/removal of united atoms to a segment is independent of the segment length. However, our simulation suggested that μ_n is strongly dependent on temperature for loops, in contrast to bridges and tails, which we attribute to the effect of torsion and hence chain stiffness on short loops.

Thermodynamic and mechanical properties of the interlamellar domain have been determined at average atmospheric conditions in a range of temperatures, $P = 1\,\mathrm{atm}$ and $T \in [350, 450]\,\mathrm{K}$, namely the isobaric and isochoric heat capacity, Grüneisen coefficients, and the anisotropic thermal expansion coefficients. The latter clearly resembled melt-like behavior in the direction normal to the surface, while in-plane one observes low, crystal-like expansion. In large systems consisting of several lamellae as shown on the left in Fig. 14.1, this strong anisotropy in thermal expansion will dominate the behavior close to the crystal surface. When measuring the thermal expansion of the entire system, averaging comes into play which in turn depends most probably on the size, density, and orientation distribution of the lamellae. In that sense, the simulations performed here provide estimates for the ingredients needed in such more complex studies.

A full mechanical characterization of any material for deformations in the linear regime is given by the stiffness or compliance matrix, respectively. For the interlamellar domain at $P = 1\,\mathrm{atm}$ and $T = 435\,\mathrm{K}$, we extracted exactly these matrices, from which Young's moduli and shear moduli were determined. According to the simulations, the bulk modulus of the interlamellar domain lies between between the experimental values reported for a purely amorphous melt and the semicrystalline solid.

14.4.2 Sharp Crystal-Melt Interface

The interface between the lamellar crystals and the non-crystalline, interlamellar region was studied using the technique of the Gibbs dividing surface. In so doing, one is able isolate the effects of the interface alone, irrespective of thickness of the lamellae and, to some degree, of the interlamellar domain. Therefore, the properties attached to the sharp interface can be used in a three-component model with arbitrary composition, which accounts for the interface contribution explicitly, in addition to the crystal and melt bulk contributions.

Our simulations resulted in values for the in-plane diagonal stress components $\pi_{xx} \simeq -0.27\,\mathrm{J/m^2}$ and $\pi_{yy} \simeq -0.4\,\mathrm{J/m^2}$, which compare reasonably well with experimental values. The anisotropy is a signature of the tilted chains exiting the lamella at the {201} surface. The sign of these stresses indicates that the interface is under pressure, due to entropic effects and due to connectivity between the crystal and non-crystalline segments. The Herring equation taught us that the surface tension (i.e., Helmholtz free energy per unit area) depends strongly on the tensile strains, but is independent of shear strains in the interface plane. Furthermore, the interface internal energy, e_{int}, and its change versus temperature was studied and quantified. The latter is of interest because it enters into the "apparent" heat capacity as measured for the entire semicrystalline material.

Throughout the manuscript, we carefully specified the variables under control. In particular when taking temperature derivatives, we observed differences between keeping pressure constant or the geometry of the system. We point out that such book keeping is essential, because it is not only responsible for quantitative differences, e.g., C_V vs. C_P, but it can even result in a alteration of the overall sign, as shown in Study 2 of the interface energy and stresses.

The internal energy and the stresses of the interface were both calculated on the basis of the respective profile obtained from our MC simulations, i.e., based on (14.10, 14.11). The way in which they are defined has clear physical meaning, as explained previously. However, one may ask about the existence of a single thermodynamic potential, namely a Helmholtz free energy of the interface, from which the internal energy and the interface stresses can be derived, in close analogy to the corresponding relations for bulk materials. Whether or not the data reported here have a chance of being derived from a single Helmholtz free energy can be discussed by testing the Maxwell relations, i.e., the relations between mixed second order derivatives of the thermodynamic potential. Doing so requires data on the strain dependence of the internal energy of the interface, which are currently not available to reasonable accuracy (see [30] for more details). Furthermore, one must realize that the thermodynamic state of the interface depends on the conditions in the two adjoining bulk phases, e.g., the pressure. Under the assumption that the difference between the surface tension γ and e_{int} equals the temperature times the entropy of the interface, s_{int}, our results for e_{int} combined with the experimental value $\gamma \sim 0.1\,\mathrm{J/m^2}$ for the fold surface [20, 21] leads to $Ts_{\mathrm{int}} \simeq 0.2\,\mathrm{J/m^2}$. However, due to the difficulties just mentioned this number should be used with caution.

14.4.3 Perspectives

Measurements of the interlamellar domain and interface, as presented here, develop their full strength when put in a wider context and combined with the material properties of the adjoining phases, e.g. the effect of the internal energy of the interface on the heat capacity of the semicrystalline material.

Another such example is the connection between interface stresses and crystal lattice distortion, and lamellar twisting. The latter phenomenon requires two additional ingredients, in addition to the interface stresses: Firstly, the interface stresses must occur asymmetrically at the two opposite lamella surfaces [56, 57], which can not be achieved in our simulations by construction of the simulation cell. Reasons for such asymmetries have to be found on different grounds. Secondly, lamellar twisting can only be predicted if also the material properties of the crystalline lamellae are incorporated, either based on experimental [58, 59] or simulated data [60].

Table 14.3 summarizes the most important results of our MC simulations in terms of thermal and mechanical properties. It is striking that no mechanical response data, e.g., stiffness or compliance data, are available for the sharp interface. In that respect we mention that measuring the change in the interface stresses with respect to small deformations (tensile, shear) in directions of the interface plane with reasonable accuracy is difficult, as discussed in more detail in [30]. However, we have the feeling that such data would be useful for calculating the average mechanical response of semicrystalline polyethylene, in conjunction with similar data for the melt and crystal phases [60] and appropriate multiphase models.

Acknowledgment

This work has been supported by the Swiss National Science Foundation under Grant Number 81EZ-68591, by the ERC program of the National Science Foundation under Grants 0079734 and EEC-9731680 (Center for Advanced Engineering Fibers and Films – CAEFF), and by the MRSEC Program of the National Science Foundation under Award Number DMR-9808941.

References

[1] R. Seguela: J. Polym. Sci. Pol. Phys., **43**, 1729 (2005)
[2] G.R. Strobl, W. Hagedorn: J. Polym. Sci B **16**, 1181 (1978)
[3] C.C. Naylor, R.J. Meier, B.J. Kip, K.P.J. Williams, S.M. Mason, N. Conroy, D.L. Gerrard: Macromolecules **28**, 2969 (1995)
[4] R.H. Boyd: Polymer **26**, 1123 (1985)
[5] C. Alvarez, I. Šics, A. Nogales, Z. Denchev, S.S. Funari, T.A. Ezquerra: Polymer **45**, 3953 (2004)
[6] S. Torquato: *Random Heterogeneous Materials* (Springer, New York, 2002)
[7] M. Hütter: Phys. Rev. E **64**, 011209 (2001)
[8] M. Hütter, G.C. Rutledge, R.C. Armstrong: Phys. Fluids **17**, 014107 (2005)
[9] E.H. Kerner: Proc. Phys. Soc. Lond. **69B**, 808 (1956)
[10] S. Uemura, M. Takayanagi: J. Appl. Pol. Sci. **10**, 113 (1966)
[11] R.M. Christensen: J. Mech. Phys. Solids **38**, 379 (1990)
[12] R.M. Christensen, K.H. Lo: J. Mech. Phys. Solids **27**, 315 (1979)

[13] S.D. Gardner, C.U.Jr. Pittman, R.M. Hackett: Compos. Sci. Technol. **46**, 307 (1993)
[14] B. Crist, C.J. Fisher, P.R. Howard: Macromolecules **22**, 1709 (1989)
[15] J. Rault: J. Macromol. Sci. Phys. **B12**, 335 (1976)
[16] R.C. Cammarata, R.K. Eby: J. Mater. Res. **6**, 888 (1991)
[17] H.P. Fisher, R.K. Eby, R.C. Cammarata: Polymer **35**, 1923 (1994)
[18] R.C. Cammarata, K. Sieradzki: Annu. Rev. Mater. Sci. **24**, 215 (1994)
[19] P.D. Calvert, D.R. Uhlmann: J. Polym. Sci. **11**, 457 (1973)
[20] B. Wunderlich: *Macromolecular Physics* (Academic Press, New York, 1976)
[21] J.D. Hoffman: Polymer **23**, 656 (1982)
[22] S. Balijepalli, G.C. Rutledge: J. Chem. Phys. **109**, 6523 (1998)
[23] S. Balijepalli, G.C. Rutledge: Macromol. Symp. **133**, 71 (1998)
[24] S. Balijepalli, G.C. Rutledge: Comput. Theor. Polym. Sci. **10**, 103 (2000)
[25] S. Gautam, S. Balijepalli, G.C. Rutledge: Macromolecules **33**, 9136 (2000)
[26] P.J. in 't Veld, G.C. Rutledge: Macromolecules **36**, 7358 (2003)
[27] G.C. Rutledge: J. Macromol. Sci. Phys. **B41**, 909 (2002)
[28] P.G. Debenedetti: *Metastable Liquids: Concepts and Principles* (Princeton University Press, Princeton NJ, 1996)
[29] P.J. in 't Veld, M. Hütter, G.C. Rutledge: Macromolecules **39**, 439 (2006)
[30] M. Hütter, P.J. in 't Veld, G.C. Rutledge: Polymer **47**, 5494 (2006)
[31] D.C. Bassett, A.M. Hodge: Proc. R. Soc. Lond. A **377**(1768), 25 (1981)
[32] W. Paul, D.Y. Yoon, G.D. Smith: J. Chem. Phys. **103**, 1702 (1995)
[33] K. Bolton, S.B.M. Bosio, W.L. Hase, W.F. Schneider, K.C. Hass: J. Chem. Phys. B **103**, 3885 (1999)
[34] N. Waheed, M.S. Lavine, G.C. Rutledge: J. Chem. Phys. **116**, 2301 (2002)
[35] M.J. Ko, N. Waheed, M.S. Lavine, G.C. Rutledge: J. Chem. Phys. **121**, 2823 (2004)
[36] M. Vacatello, G. Avitabile, P. Corradini, A. Tuzi: J. Chem. Phys. **73**, 548 (1980)
[37] R.H. Boyd: Macromolecules **22**, 2477 (1989)
[38] K.V. Pant, D.N. Theodorou: Macromolecules **28**, 7224 (1995)
[39] L.R. Dodd, T.D. Boone, D.N. Theodorou: Mol. Phys. **78**, 961 (1993)
[40] V.G. Mavrantzas, T.D. Boone, E. Zervopoulou, D.N. Theodorou: Macromolecules **32**, 5072 (1999)
[41] D.A. Kofke: J. Chem. Phys. **117**, 6911 (2002)
[42] J.D. Hoffman, R.L. Miller: Polymer **38**, 3151 (1997)
[43] M. Parrinello, A. Rahman: J. Appl. Phys. **52**, 7182 (1981)
[44] P.J. Flory, D.Y. Yoon, K.A. Dill: Macromolecules **17**, 862 (1984)
[45] A.W. Neumann, J.K. Spelt (eds.): *Applied Surface Thermodynamics* (Marcel Dekker, New York, 1996)
[46] J.B. Hudson: *Surface Science : An Introduction* (John Wiley, New York, 1998)
[47] A. Zangwill: *Physics at Surfaces* (Cambridge University Press, New York, 1988)
[48] J.W. Gibbs: *The Scientific Papers of J. Willard Gibbs*, vol. 1 (Longmans-Green, London, 1906)
[49] C. Herring: The use of classical macroscopic concepts in surface energy problems. In: *Structure and Properties of Solid Surfaces* ed by R. Gomer and C.S. Smith (The University of Chicago Press, Chicago, 1953) pp. 5–72
[50] M.P. Allen, D.J. Tildesley: *Computer Simulation of Liquids* (Clarendon Press, Oxford, 1986) Ch. 2
[51] U. Gaur, B. Wunderlich: J. Chem. Phys. Ref. Data **10**, 119 (1981)

[52] O. Olabisi, R. Simha: Macromolecules **8**, 206 (1975)
[53] J.F. Nye: *Physical Properties of Crystals* (Clarendon Press, Oxford, 1985)
[54] T. Krigas, J.M. Carella, M.J. Struglinski, B. Crist, W.W. Greassley, F.C. Shilling: J. Polym. Sci., Polym. Phys. Ed. **23**, 509 (1985)
[55] R.A. Orwoll, P.J. Flory: J. Am. Chem. Soc. **89**, 6814 (1967)
[56] H.D. Keith, F.J.Jr. Padden: Polymer **25**, 28 (1984)
[57] B. Lotz, S.Z.D. Cheng: Polymer **46**, 577 (2005)
[58] I.M. Ward: *Mechanical Properties of Solid Polymers* (Wiley, Chichester [etc.], 1983)
[59] D.T. Grubb: Elastic properties of crystalline polymers. In: *Materials Science and Technology*, Volume 12: Structure and Properties of Polymers, ed by R.W. Cahn, P. Haasen and E.J. Kramer (VCH, Weinheim [etc.], 1993) pp. 301–356
[60] G.C. Rutledge: Modeling Polymer Crystals. In *Simulation Methods for Polymers*, ed by M. Kotelyanskii and D.N. Theodorou (Marcel Dekker, New York, 2004), Ch. 9